A Synchronous Homopolar Machine for High-Speed Applications

Perry Tsao, Matthew Senesky, and Seth Sanders
Department of Electrical Engineering
University of California, Berkeley
Berkeley, CA 94720
www-power.eecs.berkeley.edu

Abstract— **The design, construction, and test of a high-speed synchronous homopolar motor/alternator, and its associated high efficiency six-step inverter drive for a flywheel energy storage system are presented in this paper. The work is presented as an integrated design of motor, drive, and controller. The performance goal is for power output of 30 kW at speeds from 50 kRPM to 100 kRPM. The machine features low rotor losses, high efficiency, construction from robust and low cost materials, and a rotor that also serves as the energy storage rotor for the flywheel system. The six-step inverter drive strategy maximizes inverter efficiency, and the sensorless controller works without position or flux estimation. A prototype of the flywheel system has been constructed, and experimental results for the system are presented.**

Keywords—Homopolar machine; Flywheel energy storage; Six-step drive; Sensorless control

I. INTRODUCTION

The design, construction, and test of a synchronous homopolar motor/alternator for a flywheel energy storage system is described in this paper. In contrast to most flywheel systems, the same rotor is used for both the motor/alternator and energy storage functions to reduce the system complexity. In addition, the functions of the vacuum housing and burst containment are both served by the stator housing. The resulting system is robust, uses low cost materials, and is simple to manufacture; yet it still maintains power and energy storage densities suitable for power quality, uninterruptible power supply, or hybrid electric vehicle applications.

The first part of the paper presents a description of the synchronous homopolar machine, machine design issues, motivation for the six-step drive strategy, and details of the prototype construction. The second part focuses on machine dynamics and controller synthesis, and presents simulations and experimental results for the control system. Finally, experimental performance results are reported and discussed, and an analysis of harmonic currents and associated copper and rotor losses is given in the appendices.

This work was supported by NSF grant number ECS-9906607, and a grant from the University of California Energy Institute (UCEI) Energy Science and Technology Program.

TABLE I. MACHINE DESIGN PARAMETERS

Power	30 kW
RPM	50kRPM- 100kRPM
Energy storage capacity	140 W.hr
System mass	36 kg
Power density	833 W/kg
Energy density	3.9 W.hr/kg

II. SYNCHRONOUS HOMOPOLAR MACHINE DESIGN

A. Application Requirements

High efficiency, low rotor losses, and a robust rotor structure are the key requirements for the flywheel system's motor/alternator. High efficiency is required over the entire range of operation, in this case 50,000 to 100,000 RPM, with a power rating of 30 kW. In addition, the zero power spinning losses of the machine must be very low. The design goals for the machine presented here are shown in Table I.

Because the rotor operates in a moderate vacuum (~0.5 mm Hg), the main paths for heat transfer from the rotor are through radiation and through the bearings (if ball bearings are used). The amount of heat transfer through radiation is small except at high temperatures, and the thermal path through the bearings is minimal, if nonzero. Limiting the rotor temperature is critical to operation; therefore, it is important to minimize

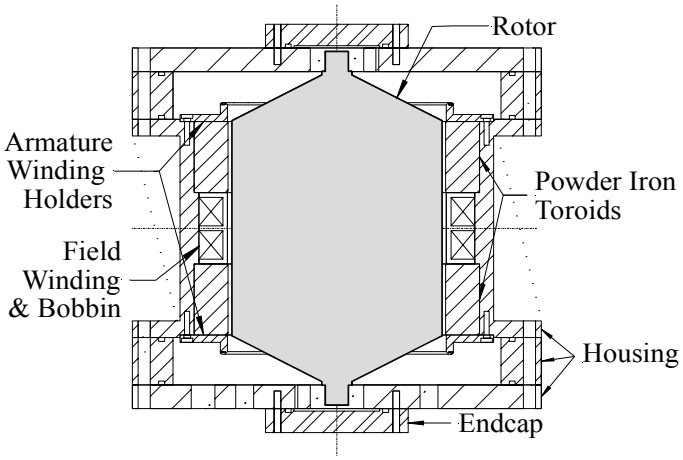

Fig. 1. Cut-away view of synchronous homopolar motor with arrows indicating magnetizing flux path.

0-7803-7420-7/02/$17.00 © 2002 IEEE

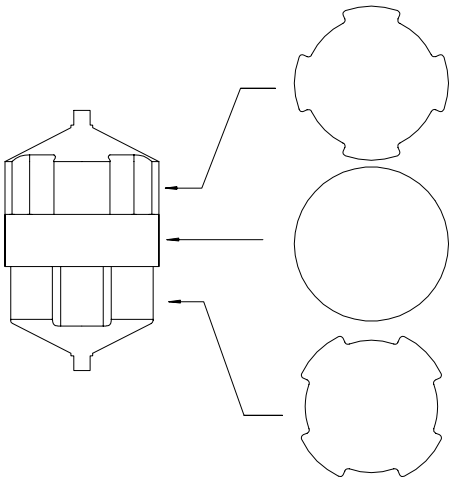

Fig. 2. View of rotor structure.

losses on the rotor. This rules out machines such as induction machines and switched reluctance machines because of their respective conduction and core losses on the rotor.

The rotor must be able to withstand the stresses of spinning at high-speed. This requirement makes the use of permanent magnets on the rotor difficult because of their brittleness and low strength. Permanent magnets are further limited by their temperature restrictions. Another important consideration is that rotor structures with multiple parts are more difficult to balance and are more likely to have unwanted vibration modes in the target operating speed range.

B. Synchronous Homopolar Motor Characteristics

Although not widely used in practice, synchronous homopolar motors have been researched for a variety of applications. They are sometimes referred to as 'homopolar inductor alternator/motors' [1,2], or simply as 'homopolar motors' [3,4]. The defining feature of these motors is the homopolar d-axis magnetic field created by a field winding [1,2,4,5,6], permanent magnets, or a combination of permanent magnets and windings [3]. The principle is the same as in a traditional synchronous generator, with which the synchronous homopolar motor has similar terminal characteristics. However, in the case of the synchronous homopolar motor the field winding is fixed to the stator and generally encircles the rotor rather than being placed on the rotor. The field winding and the magnetizing flux path in the present motor design are shown schematically in Fig. 1. Note that the rotor pole faces on the upper part of the rotor are offset from the pole faces on the lower part (see Figs. 2 and 12).

There are several advantages to having the field winding in the stator. Among these are elimination of slip rings and greatly simplified rotor construction, making it practical to construct the rotor from a single piece of high strength steel. This feature makes homopolar motors very attractive for high-speed operation; a single piece steel rotor is used in the design presented here and in [1,5,6]. The other rotor designs feature laminations [4], permanent magnets [3], or other non-magnetic structural elements to increase strength and reduce windage losses [2]. Additional advantages of having the field winding in the stator include ease in cooling the field winding and increased volume available for this winding. The large volume available for the field winding allows high flux levels to be achieved efficiently, making a slotless stator design feasible.

The slotless stator makes the synchronous homopolar motor even better suited for high-speed solid rotor designs because it eliminates slotting induced rotor losses that might otherwise incur rotor losses [7]. A slotless stator also allows for higher gap flux densities because saturation of the stator teeth is no longer a concern. The design principle is similar to a slotless permanent magnet machine, with the advantage that the magnetizing field can be controlled to keep efficiency high at low and zero torque.

A possible disadvantage of the slotless stator is the difficulty in constructing the armature winding, which must be bonded to the smooth inner bore of the stator iron. As described in section II-*E*, a relatively simple and effective process was developed to construct the winding in the prototype.

C. Design Optimization

A constrained optimization was used to maximize efficiency for a machine meeting the power rating and energy storage capacity listed in Table I. Essential machine parameters (e.g. rotor radius, rotor length, air gap, field winding volume) were used to calculate the power output, energy storage, and efficiency of each design. Included in the optimization were lumped parameter calculations of the magnetic paths, mechanical calculations for the rotor's natural frequency and maximum stresses, conduction losses, and core losses. Performance requirements and physical limitations such as saturation flux and peak rotor stresses were implemented as constraints on the design optimization.

The first step in the optimization process was to choose rotor dimensions that would meet the energy storage capacity goal of 500 kJ (140 W.hr). The energy storage capacity of the rotor is determined to first order by the strength-to-weight ratio of the rotor material and the rotor mass [8]. Rotor shape and a safety margin further influence the energy storage capacity. Thus, the rotor mass is largely determined by the energy storage objective and the rotor material. It is assumed that the flywheel operates in a speed range of $\frac{1}{2}*\varpi_{max}$ to ϖ_{max}, which implies that ¾ of the maximum kinetic energy can be recovered. Additional factors considered in the rotor selection include the first bending mode, the ratio of principle moments of inertia, and rotor saliency. The first bending mode (natural frequency) was calculated to ensure that it is above the target operating range. Rotor shapes where the rotational moment of inertia and the longitudinal moment of inertia were roughly equal were selected to minimize the possible effects of rotor unbalance moments [9].

The second optimization step was to run a local optimization for each candidate rotor that optimized the machine design for that particular rotor. A lumped parameter model was used in the local optimization to find the optimal

air gap, pole face arcs, armature and field coil winding volume, and currents in the stator armature and field windings to minimize losses at the worst case operating point. A range of candidate rotor shapes was found using these criteria to consider for further optimization. The constraints on the local optimization required a power output of 30 kW for the target speed range of ½*ϖ_{max} to ϖ_{max}, and a peak flux density below saturation (1.5 Tesla). The results of the local optimizations were used to pick an initial design, and after the initial design was completed, an actual winding design was done to calculate more accurate parameters and make refinements to the optimized model. Parameters for the resulting design are reported in Tables II and III. Performance curves which break down loss components over the 50-100 kRPM speed range for 5, 15, and 30 kW power levels are reported in Fig. 3. These curves are calculated based on the six-step drive strategy detailed in the next section. Note that for a fixed-voltage drive the efficiency remains roughly constant for higher power levels, but drops at lower power levels. To avoid operating at lower efficiency operating points, the flywheel could be operated in pulse mode when average power levels below 5kW are necessary.

TABLE II. OPTIMIZATION RESULTS

An important part of the design process was the optimization of the worst-case efficiency, which occurs at full power at the lowest operating speed. In the case of the present design, this corresponds to determining the optimal armature and field winding currents at 30 kW and 50 kRPM. Generally, these operating points occurred at unity machine power factor, where the motor currents are in phase with the back emf of the field winding flux. This observation motivated the selection of a drive strategy that runs near unity machine power factor.

Optimized Parameter	Value
Rotor diameter	11.2 cm
Rotor length	11.5 cm
Rotor inertia	0.0124 kg/m^2
Magnetic gap	0.216 cm
Field winding ID, OD, height	11.5 cm, 15 cm, 3.8 cm
Armature winding thickness	0.130 cm
L_d	113 µH
L_d/L_q *ratio*	1
L_M	1.35 mH
Worst-case efficiency 50 kRPM, 30 kW	93%

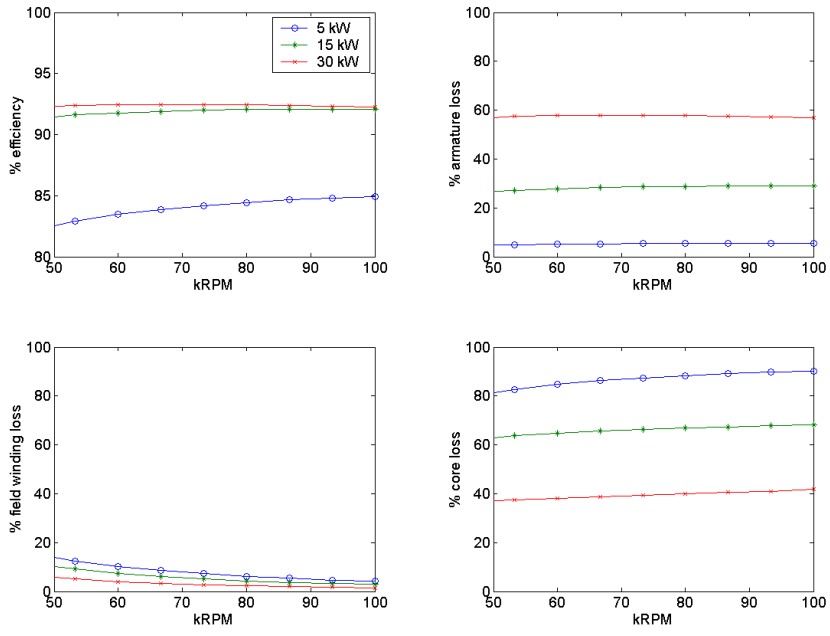

Fig. 3. Machine design efficiency with constant bus voltage.

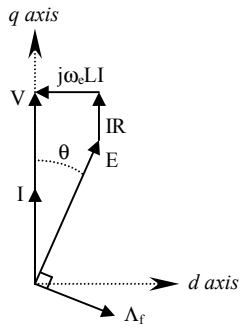

Fig. 4. Motor vector diagram.

D. *Six-step Drive Strategy*

The drive of a high-speed synchronous homopolar machine presents some unique challenges. The high electrical frequencies (6.6 kHz at 100 kRPM) make a standard PWM drive scheme impractical. Drive efficiency is also a concern; we wish to minimize switching loss in the inverter, conduction loss in both the inverter and the machine, and core loss in the machine. In consideration of the above issues, a six-step inverter drive operating at unity inverter power factor from a fixed, unregulated DC bus was selected for the excitation of the synchronous homopolar machine.

A six-step drive scheme is attractive for both switching and inverter conduction loss considerations. The maximum switching frequency for any one switching element is the machine's maximum electrical frequency, in this case 6.6 kHz. This frequency is relatively low for modern IGBT technology. Note that for six-step drives, zero-current switching (ZCS) occurs when operating at unity inverter power factor. This is in contrast to PWM, which is difficult to implement at the targeted drive frequencies, has much higher switching frequencies, and neither ZVS nor ZCS.

Operating at unity inverter power factor minimizes currents for a given electrical input power, which reduces the VA requirements, and hence cost, for the semiconductor elements. Conduction losses are also low, because at this operating point the losses are determined roughly by the ratio of the forward conduction voltage drop of an inverter device to that of the back emf. This can easily fall in the range of 1%. The unity inverter power factor operating point is also advantageous for motor operation. Although unity inverter power factor and unity machine power factor (the optimal operating point determined in the design optimization) are different operating points, they are close together since the back emf E and the applied voltage V are much larger than the inductive voltage drop $j\omega_e LI$, as illustrated in Fig. 4. Note that the orientation of the d-q axes in Fig. 4 where the q-axis coincides with the voltage

vector is non-standard. The rationale for this choice of axis orientation is described in Section III-A.

In summary, the choice of a six-step inverter drive operating at unity inverter power factor is nearly optimal for machine efficiency, reduces switching losses (vs. PWM), and minimizes inverter conduction losses. The last consideration is core loss, which we believe will not be significantly higher when compared to a sinusoidal drive. The six-step drive precludes all triple-n harmonics with an open neutral connection; thus, the main time harmonics seen by the machine are the fifth and seventh harmonics. As noted in [10,11], six-step waveforms result in only slightly higher core losses than those achieved with sinusoidal waveforms in induction machine drives, and we believe that those results also carry over to the stator core losses in the machine discussed here. In appendices A-I through A-IV, we show that with proper sizing of the phase inductance L_A, the harmonic conduction and rotor losses are small.

TABLE III. PROTOTYPE PARAMETERS

Rotor Parameters		Stator Parameters	
Material	4340 Steel	***Core Material***	MII Technologies SM-2HB
Diameter	11.2 cm	***Stator Length***	11.5 cm
Length	11.5 cm	***Housing Dimensions***	22cm x 22cm x 22cm
Mass	9.5 kg (21 lbs)	***Housing Volume***	10,650 cm^3

E. Prototype Construction

The dimensions, and other important parameters for the prototype are shown in Tables II and III. The rotor for the machine consists of a single piece of high strength steel. As shown in Fig. 2, four poles are cut into both the upper and lower parts of the rotor with the lower poles rotated 45 degrees with respect to the upper poles. The center portion of the rotor is cylindrical, and the field winding encircles this portion of the rotor. The four upper poles are all the same magnetic polarity (N), and the flux returns down through the backiron to the lower set of poles (S). The machine has 8-poles, and no saliency, i.e. $L_d/L_q \approx 1$.

The stator is made from powder iron material from MII Technologies [15]. The powder iron material is specified to have lower loss than M19 24 gauge laminations at the machine's operating electrical frequencies. The powder iron is formed into a toroid with a rectangular cross-section, and is press-fit into a steel tube that serves as both the back iron and housing for the machine. Only the field winding flux and not the alternating flux of the armature travels through the back iron, so core loss in the back iron is not an issue. The field winding was wound around a bobbin and also pressed into the backiron. An aluminum bobbin was used for thermal and structural considerations.

The most challenging part of the prototype construction was the winding of the stator armature. The armature was formed from rectangular Litz wire bonded to the inner bore using thin sheets of FR4 prepreg. FR4 prepreg is the half-cured form of the yellow-green epoxy-fiberglass laminate commonly used as printed circuit board substrate. The type of FR4 employed here was very thin (roughly 13μm or 0.0005").

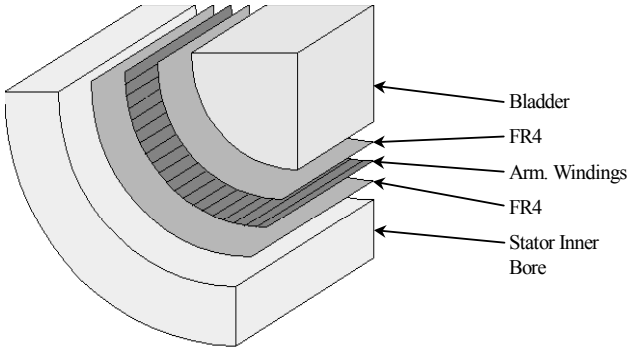

Fig. 5. Slotless winding construction. Cutaway view of ¼ of stator.

A diagram of the construction assembly is shown in Fig. 5. First, a layer of FR4 was placed against the inner bore, followed by the windings, and then an additional layer of FR4 on the inside of the windings. Then an air bladder was inserted and inflated to ~1 atm. (15 psi.) to compress the FR4-Litz wire-FR4 assembly against the inner bore. The stator assembly was then baked in an oven to reflow and fully cure the epoxy in the FR4. After baking, the air bladder was removed, and the result was a smooth and solid winding structure bonded tightly to the inner bore of the motor. Photos of the completed armature are shown in Figs. 13 and 14.

Fig. 6. Tolerance ring.

A compliant bearing mount was also designed and built to allow the rotor to operate at speeds above resonance. The first resonant mode was designed in the range of 20 kRPM. The mount consisted of a 'tolerance ring' [16] clamped around the outside of the bearing, and compressed into a bore. The tolerance ring, shown in Fig. 6 is a band of spring steel with ridges that flex to provide compliance.

III. DYNAMICS AND CONTROL

A. Machine Model

The synchronous homopolar motor has the same terminal characteristics as a traditional field-wound synchronous machine. Using a two-phase stator model, we have two orthogonal armature windings whose orientations are denoted as axes *a* and *b*. A field winding along the rotor axis *f* has mutual inductance with the armature; this inductance varies with the angle ϕ between the *a* and *f* axes. Thus in a stationary reference frame we have the two-axis model

$$\tfrac{d}{dt}\lambda_{abf} = -\mathbf{R}\mathbf{L}^{-1}\lambda_{abf} + V_{abf} \tag{1}$$

where

$$\mathbf{R} = \begin{bmatrix} R & 0 & 0 \\ 0 & R & 0 \\ 0 & 0 & R_f \end{bmatrix} \tag{2}$$

$$\mathbf{L} = \begin{bmatrix} L & 0 & L_m \cos\phi \\ 0 & L & -L_m \sin\phi \\ L_m \cos\phi & -L_m \sin\phi & L_f \end{bmatrix} \quad (3)$$

The mechanical frequency of the rotor is governed by

$$\tfrac{d}{dt}\omega_m = -\tfrac{B}{J}\omega_m + \tfrac{1}{J}\tau_e \quad (4)$$

where J is the inertia of the rotor, B represents linear drag, and τ_e is electrical torque given by

$$\tau_e = \tfrac{1}{2}\lambda^T \mathbf{L}^{-1}\lambda \quad (5)$$

It is advantageous to transform the equations into a synchronous reference frame. The natural choice of input for our six-step drive scheme is the inverter electrical frequency ω_e, so we choose to orient the q axis with the armature voltage vector. As a consequence, V_q is constant, and V_d is identically zero. A high-bandwidth current control loop is implemented to set i_f, allowing the dynamics of λ_f drop out of the model. Under these conditions, the electrical dynamics simplify to

$$\tfrac{d}{dt}\lambda_d = -\tfrac{R}{L}\lambda_d + \omega_e\lambda_q + \tfrac{RL_m}{L} i_f \cos\theta \quad (6)$$

$$\tfrac{d}{dt}\lambda_q = -\omega_e\lambda_d - \tfrac{R}{L}\lambda_q - \tfrac{RL_m}{L} i_f \sin\theta + V_q \quad (7)$$

$$\tfrac{d}{dt}\theta = \omega_e - 4\omega_m \quad (8)$$

where (8) describes the evolution of the angle, θ, between the reference frame and the rotor. Finally, we are interested in the outputs i_d and i_q:

$$i_d = \tfrac{1}{L}\lambda_d - \tfrac{L_m}{L} i_f \cos\theta \quad (9)$$

$$i_q = \tfrac{1}{L}\lambda_q + \tfrac{L_m}{L} i_f \sin\theta \quad (10)$$

Since the principle function of the flywheel energy storage system is as an electrical energy reservoir, we wish to control the flow of electrical power into and out of the machine rather than a mechanical quantity such as torque or speed. Our strategy for this is to focus on the electrical variables, developing instantaneous control of electrical power flow, considering the speed to vary slowly. The effect of extracting or supplying power to the machine is to decelerate or

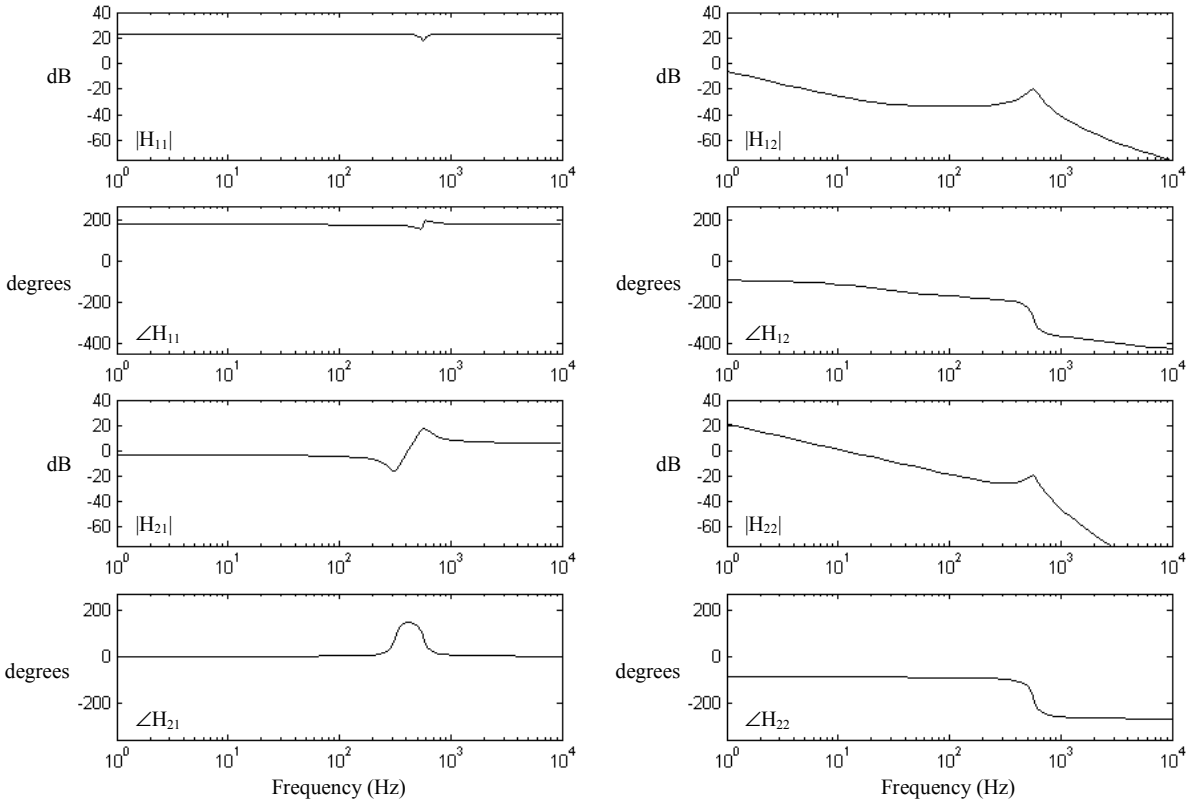

Fig. 7. Frequency response of linearized system.

TABLE IV. TRANSFER FUNCTIONS FOR LINEARIZED SYSTEM

$$H_{11} = -\left(\tfrac{L_m}{L}\cos\theta\right)\frac{s^2 + \tfrac{R}{L}s + \omega_e^2 + \omega_e\tfrac{R}{L}\tan\theta}{s^2 + 2\tfrac{R}{L}s + \left(\tfrac{R}{L}\right)^2 + \omega_e^2}$$

$$H_{12} = \frac{i_q s^2 + \left(\tfrac{R}{L}i_q - \tfrac{1}{L}\omega_e\lambda_d\right)s + \omega_e^2\left(i_q - \tfrac{1}{L}\lambda_q\right) + \omega_e\tfrac{R}{L}\left(i_d - \tfrac{1}{L}\lambda_d\right)}{s(s^2 + 2\tfrac{R}{L}s + \left(\tfrac{R}{L}\right)^2 + \omega_e^2)}$$

$$H_{21} = \left(\tfrac{L_m}{L}\sin\theta\right)\frac{s^2 + \tfrac{R}{L}s + \omega_e^2 - \omega_e\tfrac{R}{L}\cot\theta}{s^2 + 2\tfrac{R}{L}s + \left(\tfrac{R}{L}\right)^2 + \omega_e^2}$$

$$H_{22} = \frac{-i_d s^2 - \left(\tfrac{R}{L}i_d + \tfrac{1}{L}\omega_e\lambda_q\right)s - \omega_e^2\left(i_d - \tfrac{1}{L}\lambda_d\right) + \omega_e\tfrac{R}{L}\left(i_q - \tfrac{1}{L}\lambda_q\right)}{s(s^2 + 2\tfrac{R}{L}s + \left(\tfrac{R}{L}\right)^2 + \omega_e^2)}$$

accelerate the rotor, respectively. Explicitly, real power is controlled by regulating i_q, while reactive power is controlled by regulating i_d.

For consideration of the electrical power flow, we treat the speed as a constant parameter. A more formal analysis would rely on singular perturbation theory with speed and other mechanical variables treated as forming the "slow subsystem." We omit the details here. Holding ω_m constant and performing a small signal linearization of the electrical subsystem about a desired operating point, we obtain a linear state-space model for the electrical subsystem. We then compute the transfer function matrix $H(s)$, partitioned as:

$$\begin{bmatrix} i_d \\ i_q \end{bmatrix} = \begin{bmatrix} H_{11} & H_{12} \\ H_{21} & H_{22} \end{bmatrix} \begin{bmatrix} i_f \\ \omega_e \end{bmatrix} \tag{11}$$

where the functions H_{11}, H_{12}, H_{21}, and H_{22} are given in Table IV.

Bode plots of these functions are shown in Fig. 7. Table V gives the operating point values used to generate the plots. Note that at low frequencies the magnitude of the diagonal terms is larger than that of the off-diagonal terms. Although for clarity we only plot results for one operating point, the qualitative relationship among the magnitudes of the four terms holds over a wide range of operating points. This carries important consequences for our control, as discussed in the next subsection.

TABLE V. SMALL SIGNAL OPERATING POINT

Parameter	Value
V	26 V
θ	7.9°
ω_e	3522 rad/s
i_d	0 A
i_q	10 A
i_f	4.9 A
λ_d	7.3e-3 Wb
λ_q	0 Wb

B. Control Design

The objective in designing a controller is to stabilize the system for operating points near unity power factor, and to be able to track a command for real power. As the excitation voltage is fixed, this amounts to controlling i_q to a reference value while keeping i_d at zero.

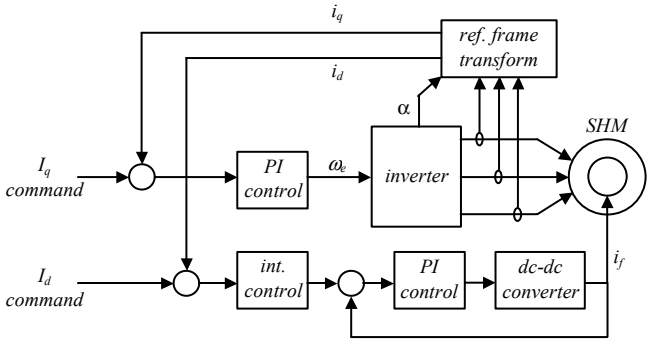

Fig. 8. Control system block diagrram

Intuition for the operation of the system at or near unity power factor can be gained by examining the phasor diagram in Fig. 4. Note that the figure is not drawn to scale; over the desired range of operating points, the angle θ will be small, and the effect of resistive drop will be negligible. Letting $\sin(\theta) \approx \theta$, steady-state i_q varies nearly linearly with θ (and hence the integral of ω_e) with little effect on i_d. Similarly, adjusting the magnitude of the back-emf E controls steady state i_d with little effect on i_q. These are the standard relations for a synchronous generator connected to an infinite bus.

The Bode plots for the linearized system shown in Fig. 7 confirm the intuition for DC values, and provide insight into the dynamics of the electrical states. It can be shown that for the purposes of the control scheme, it is the relative magnitudes of the quantities $|H_{11}H_{22}|$ and $|H_{12}H_{21}|$ that determine whether the system can be considered decoupled. Adding the log magnitudes from the figure, we see that $|H_{11}H_{22}|$ is greater than $|H_{12}H_{21}|$ by roughly 50 dB at low frequencies.

Given the largely decoupled nature of the system, we can construct two independent control loops, as shown in the block diagram in Fig. 8. An integral control law for the $i_d \rightarrow \omega_e$ loop ensures that the power factor is driven to unity. A PI control on the $i_q \rightarrow \omega_e$ loop provides the desired response for tracking the commanded active current. A nested current control loop for the field winding is also implemented. Table VI, showing the resulting closed-loop poles for the linearized system, confirms that the control indeed stabilizes the system at the desired operating point.

TABLE VI. CLOSED-LOOP POLES

-334.5 ± 3521.5j
-189.2 ± 3514.3j
-273.6
-37.1
-16.6

An attractive feature of the control scheme is its simplicity. Unlike flux-oriented schemes, the controller does not require an observer to resolve the reference frame. The reference frame angle α is defined by the inverter voltage; by triggering the control loop from the inverter switching, the angular orientation of the reference frame is known explicitly. Furthermore, because the magnitude of the excitation voltage is fixed, it is only necessary to sample the armature currents. Note that while field current is also sampled to implement a separate current control loop, this sampling is not fundamentally necessary for the overall control scheme – it is a design choice to simplify the experimental setup.

The inverter switching and the generation of a sampling interrupt are both handled by an FPGA. Samples of i_d and i_q are taken just before inverter switching occurs, so that the orientation of the current relative to inverter voltage is known. Note that this means sampling occurs at a rate of six times the electrical frequency. These samples, rotated into the synchronous reference frame, are then made available to the control loop, which performs control calculations at a fixed rate of 1.5 kHz.

C. Controller Simulation and Experimental Results

Fig. 9 shows system response to step commands from 10A to –1A, and –1A to 10A. The plots show experimental results, the current command, and simulations using the nonlinear dynamics presented in equations (4) through (8). Fig. 10 shows the inverter frequency corresponding to this power

TABLE VII. DESIGN AND MEASURED PARAMETERS

	Description	Design Value	Measured Value
L_d, L_q	2-phase inductance	113 µH	101.6 µH
L_m	Mutual inductance	1.349 mH	1.162 mH
λ_r	Rotor remnant magnetization	NA	0.0018 Wb
R_a	Phase resistance	42.0 mΩ	45.4 mΩ
R_f	Field winding resistance	3.22 Ω	3.44 Ω

trajectory, and demonstrates the controller's capability to execute constant current accelerations and decelerations.

The coupling of the i_q step into i_d is the result of coupling from i_q to V via a sag in the bus voltage under load. This effect was included in the nonlinear simulation as a simple resistive drop. It could be eliminated in the experimental setup with a stiffer bus.

IV. EXPERIMENTAL RESULTS

All experimental data was obtained with discrete inductors augmenting the machine inductance to the approximate nominal design value. Data was collected for no-load, constant-speed spin tests at various operating points and a least-squares fit was used to extract machine inductances. DC resistances were measured directly. Table VII compares the design values and fitted parameters. Parameter λ_r corresponds to the stator flux linkage due to rotor remnant magnetization.

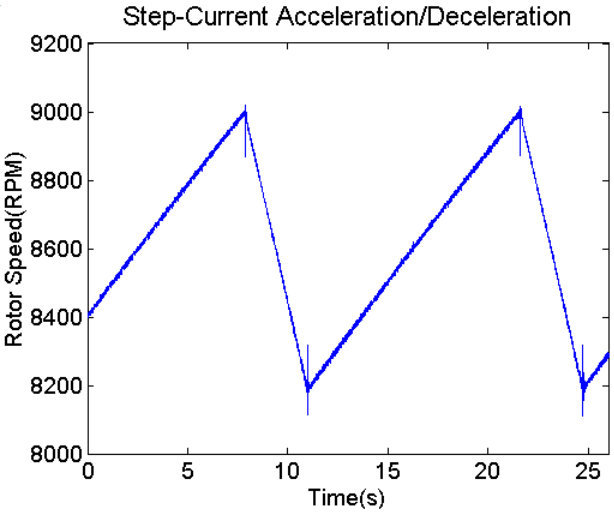

Fig. 10. Speed trajectory during step current command..

A. Performance Results

Spindown tests were conducted to measure the bearing and core losses of the motor. In the spindown tests, the motor

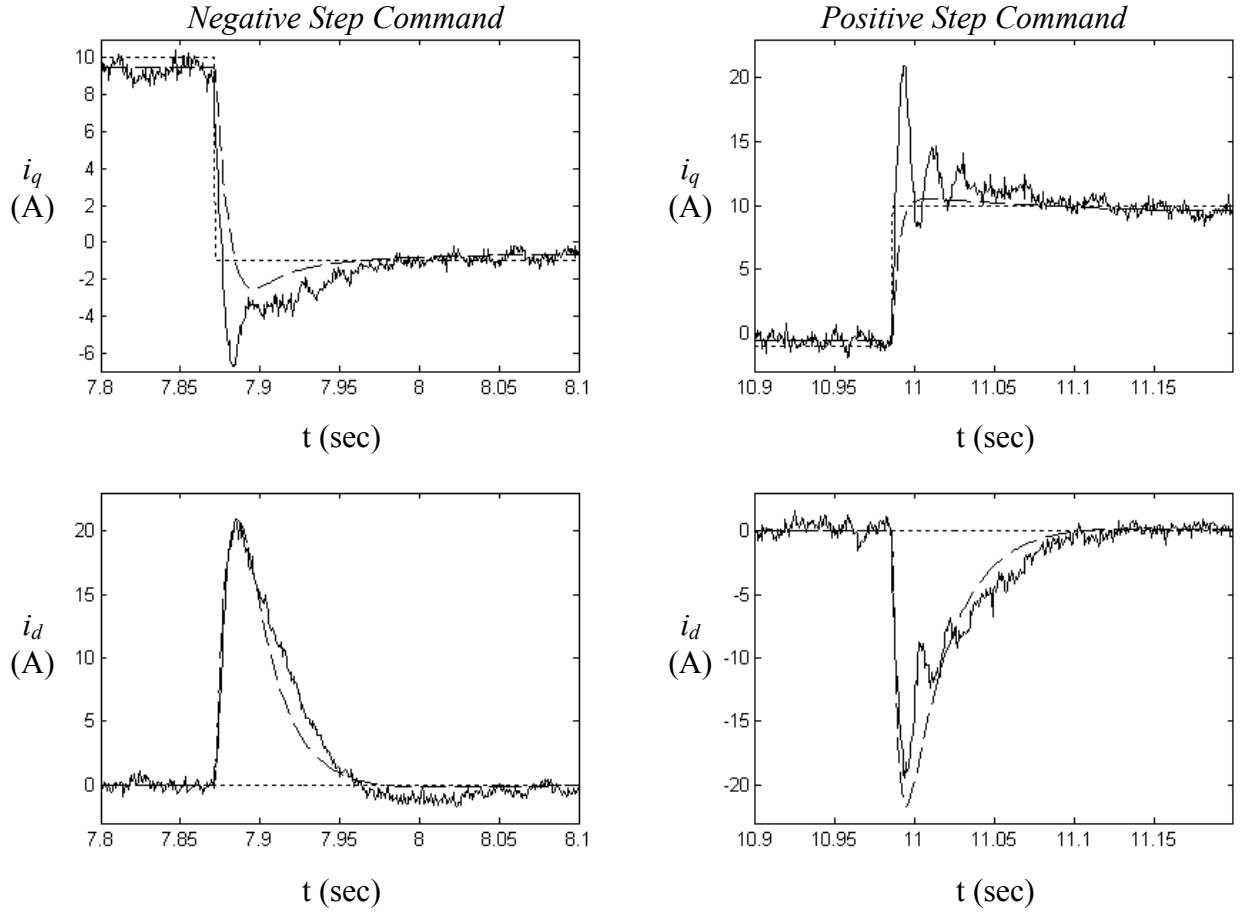

Fig. 9. Step response results. Experimental (solid line), command (dotted), and simulation (dashed).

was spun up to a certain speed, and then the armature current was cut off and the field winding was used to apply varying flux levels. The rate of spindown was used to measure the spinning losses, which are composed of bearing loss and core loss. The back-emf of the motor was also measured to calculate the flux level. These test were conducted for various flux levels up to 0.85T and speeds up to 27kRPM. A nonlinear least-square parameter fit was then used to adjust parameters for a bearing and core loss model. Fig. 11 shows the data taken and the curve generated from the curve fit.

The bearing and core loss model parameters generated from the spindown tests were then compared to other data taken at constant speeds and flux levels, as shown in Table VIII. The test conditions and measured power quantities P1, P2 are as indicated in the table. Column P1 is the total input power and column P2 is the input power into the DC/DC converter driving the field winding. The values in P3 were estimated from manufacturer data for the IGBT/diode conduction drops, and the values in CL1 were calculated by subtracting the two loss quantities from the input power P1, i.e. CL1=P1-P2-P3. The "Spindown model" columns are calculated from the operating shown under "Test conditions" and parameters generated from the spindown test curve fits. As can be seen from the table, there is reasonably good agreement between the two loss calculations even at the 30 and 50 kRPM operating points. These operating points are extrapolations for the spindown model since it is developed from data up to 27 kRPM. This suggests that the core loss and the bearing loss models generated from the spindown tests are useful.

The test data and the core loss model indicate that the motor has significantly higher core losses than expected. The core loss data reported in Table VIII is approximately 5 times higher than the data used in the design. Possible reasons include additional losses from the harmonics of the square wave rotor MMF, fringing fields inducing eddy currents in the winding bobbin, and bulk eddy currents in the stator iron. Further results have not yet been obtained because of an unexpected bearing mount failure that occurred during testing which damaged the armature windings.

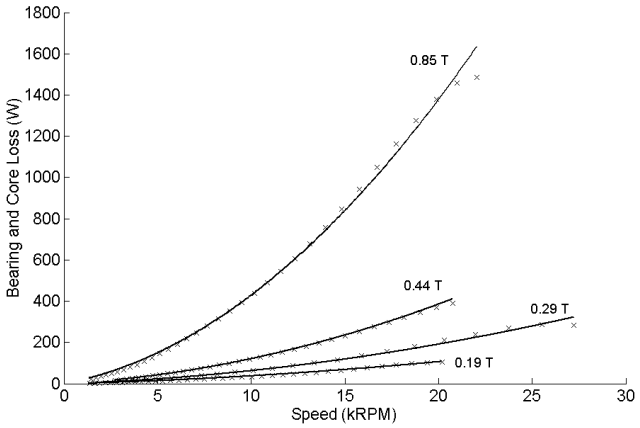

Fig. 11 Spindown test data taken at varying flux levels (x's), and bearing and core loss curve fit (solid).

B. *Bearing Mount Failure*

An inspection of the motor after the event suggests that the cause of failure was the dislodging of one of the compliant bearing mounts, either through vibration or fatigue. Once dislodged, the bearing became unseated, and the spinning rotor had enough play to come in contact with the armature and destroy the windings. Aside from the armature windings, the damage to the rest of the stator interior (including the field winding) was cosmetic, no damage was visible from the exterior, and the vacuum seals did not fail. Although certainly not conclusive, the experience suggests that the stator may provide containment for bearing failures and other rotor touchdown events.

V. CONCLUSIONS

The design and experimental results from a synchronous homopolar motor/alternator have been presented. The advantages of a slotless synchronous homopolar motor for high-speed applications are described. An analysis of rotor losses suggests that the current and winding harmonics are low enough to permit the use of a solid steel rotor.

A sensorless control scheme that does not require an

TABLE VIII. COMPARISON OF POWER MEASUREMENTS AND BEARING AND CORE LOSS MODEL

Test conditions			**Measured values**		**Calculated**		**Spindown model**			
Test speed (kRPM)	***Electrical frequency (kHz)***	***Bpk (T)***	***P1. System input power (W)***	***P2. DC/DC Input (W)***	***P3. Inverter and Cond. Loss* (W)***	***CL1. Bearing and Core Loss (W)***	***Bearing loss (W)***	***Core loss (W)***	***CL2. Bearing and Core Loss (W)***	***CL1, CL2, % difference***
22.2	1.48	0.355	382	43	14	325	50	274	324	-0.41
22.2	1.48	0.464	568	82	18	468	50	471	521	11.30
22.2	1.48	0.630	1103	170	26	907	50	877	927	2.19
22.2	1.48	0.847	2094	338	44	1712	50	1629	1679	-1.95
30.0	2.00	0.217	264	14	11	239	72	175	247	3.34
50.0	3.33	0.374	1400	57	38	1305	136	1376	1512	15.82

Fig. 12. Rotor mounted in one of the endplates.

estimator for rotor position or flux was presented. The controller is implemented as part of a six-step inverter drive strategy that minimizes conduction losses by operating at unity power factor.

Spindown tests were conducted to derive models for the bearing and core losses. The extrapolated calculations from the models agreed with further higher speed test data. Core losses were higher than anticipated. These losses may be alleviated by shifting the operating point for the motor, and/or designing with a lower loss core material such as ferrite or amorphous laminations.

The controller was demonstrated for speeds from 5,000 to 50,000 RPM. Successful operation of the rotor in the compliant mount above its first critical speed was also demonstrated, but an unexpected failure in the bearing mount did occur at 50,000 RPM. The motor is currently being repaired, and further results will be developed.

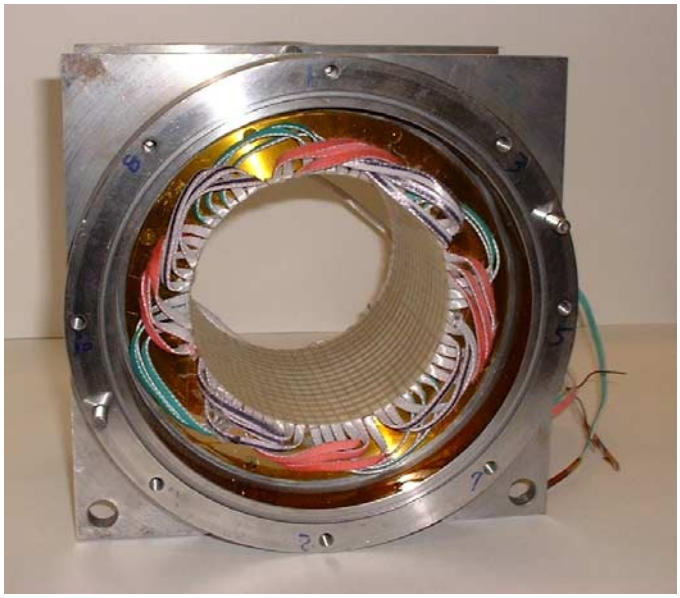

Fig. 13. View of stator and armature winding.

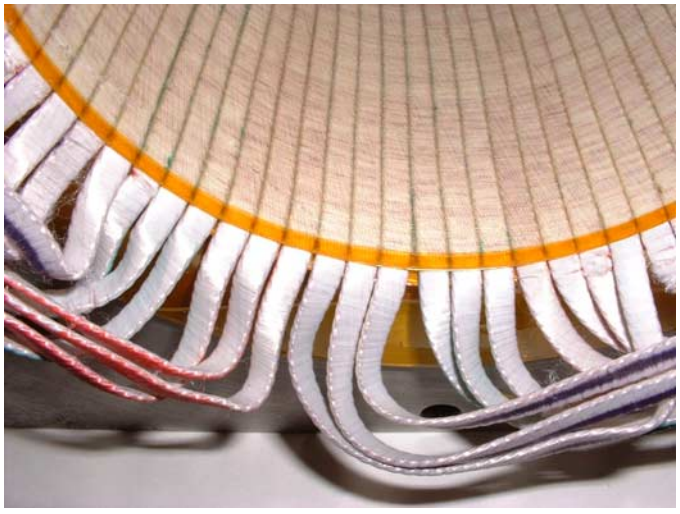

Fig. 14. Close-up view of armature winding.

ACKNOWLEDGMENTS

The authors would like to thank Warner Carlisle, Joe Gavazza, and Ben Lake of the ERL Machine Shop for their tremendous help in the construction and design of the prototype.

REFERENCES

[1] Jin He, and Feng Lin. "A high frequency high power IGBT inverter drive for 45 HP/16,000 RPM brushless homopolar inductor motor," *Conference Record of the 1995 IEEE IAS Annual Meeting,* pp.9-15.

[2] M. Siegl, and V. Kotrba, "Losses and cooling of a high-speed and high-output power homopolar inductor alternator," IEE Fifth International Conference on Electrical Machines and Drives (Conf. Publ. No.341), London, UK, 11-13 Sept. 1991 pp.295-299.

[3] G.P. Rao, J.L. Kirtley, Jr., D.C. Meeker, and K.J. Donegan. "Hybrid permanent magnet/homopolar generator and motor," U.S. Patent 6,097,124, Aug. 1, 2000.

[4] O. Ichikawa, A. Chiba, and T. Fukao. "Development of Homo-Polar Type Bearingless Motors," *Conference Record of the 1999 IEEE IAS Annual Meeting,* pp. 1223-1228.

[5] M. Hippner, and R.G. Harley, "High speed synchronous homopolar and permanent magnet machines comparative study," *Conference Record of the 1992 IEEE Industry Applications Society Annual Meeting,* pp.74-78

[6] "Cleansource 2 Flywheel Energy Storage System." Activepower, Inc. Information available online at www.activepower.com

[7] H. Hofmann, and S.R. Sanders, "High-speed synchronous reluctance machine with minimized rotor losses," *IEEE Transactions on Industry Applications,* vol. 36, No. 2, pp. 531-539, Mar. 2000.

[8] G. Genta, *Kinetic Energy Storage,* Boston: Butterworths, 1985.

[9] E. Kramer, *Dynamics of Rotors and Foundations,* New York: Springer-Verlag, 1993, pp. 66-67.

[10] A. Boglietti, P. Ferraris, M. Lazzari, and F. Profumo, "Energetic behavior of soft magnetic materials in the case of inverter supply," *IEEE Transactions on Industry Applications*, vol. 30, No. 6, pp. 1580-1587, Nov. 1994.

[11] A. Boglietti, P. Ferraris, M. Lazzari, and F. Profumo, "Energetic behaviour of induction motors fed by inverter supply," *Conference Record of the 1993 IEEE IAS Annual Meeting*, pp. 331-335

[12] A.E. Fitzgerald, C. Kingsley, S.D. Umans, *Electric Machinery*, New York: McGraw-Hill, Inc., 1990, pp. 270-271.

[13] H. Hofmann, *High-Speed Synchronous Reluctance Machine for Flywheel Applications,* Ph.D. Thesis, Dept. of EECS, University of California, Berkeley.

[14] J.R. Melcher. *Continuum Electromechanics,* Cambridge, MA: MIT Press, 1981. pp. 6.12-6.13

[15] MII Technologies *http://www.miitechnologies.com/*

[16] USA Tolerance Ring *http://www.usatolerancerings.com/*

APPENDICES

A-I. HARMONIC CURRENT CONDUCTION LOSS

The voltage on phase A of a three phase motor driven with a six-step excitation at an electrical frequency ω_e can be expressed as a sum of its Fourier components:

$$V_A = V \sum_{k=1,5,7,11,13\ldots} A_k \cos(k\omega_e t + \frac{\pi}{2}) \qquad (12)$$

where V is the fundamental of the stator excitation and $A_k=1/k$. Triple-n harmonics are assumed to be excluded by the three phase connection of the motor. Phase voltages V_B and V_C have

analogous expressions shifted by $+2\pi k/3$ and $-2\pi k/3$, respectively. Neglecting resistance, the expression for the phase currents is then:

$$I_A = V\left(\sum_{k=1,5,7,11,13\ldots} \frac{A_k}{k\cdot\omega_e\cdot L_A}\cos(k\omega_e t)\right) - \frac{E}{\omega_e\cdot L_A}\cos(\omega_e t) \quad (13)$$

where L_A is the phase inductance, and E the back emf. As evident from (13), increasing L_A decreases the amplitude of the harmonic currents and thus the associated losses. In our design, an estimate of the additional losses expressed as a fraction of the peak conduction losses is:

$$\frac{P_{harm.\,cond.}}{P_{pk.\,cond.}} \approx \frac{I_{A5}^2 + I_{A7}^2 + \ldots}{I_{A1}^2} \quad (14)$$

where I_{An} is the amplitude of the nth harmonic current in phase A, and I_{A1} is the peak current in phase A. For the worst case at 50,000 RPM where the peak current is 140 A, the additional conduction losses are less than 1%.

A-II Rotor Harmonic Loss Analysis

Since the rotor is constructed out of a single piece of solid steel, any varying flux imposed by either time or spatial harmonics will cause rotor loss and subsequent heating. Thus, care must be taken to ensure that the choice of six-step drive does not cause high rotor losses. The primary flux imposed on the rotor is the DC flux imposed by the field winding. The only time varying fluxes seen by the rotor rotating at synchronous speed are time harmonics from currents and spatial harmonics from winding geometry. The following analysis suggests that losses imposed by the current harmonics and spatial harmonics are small.

Expressing the phase currents I_A, I_B, and I_C in terms of their Fourier components as is done in (13), and applying the Park transform [12] into the synchronous frame leads to:

$$I_d = \frac{V}{\omega_e\cdot L_A}\left(\left(1-\frac{E}{V_S}\right) + \sum_{i=1,2,3\ldots}\left(\frac{A_{6i-1}}{6i-1} + \frac{A_{6i+1}}{6i+1}\right)\cos(6i\omega_e t)\right) \quad (15)$$

$$I_q = \frac{V}{\omega_e\cdot L_A}\left(\sum_{i=1,2,3\ldots}\left(-\frac{A_{6i-1}}{6i-1} + \frac{A_{6i+1}}{6i+1}\right)\sin(6i\omega_e t)\right)$$

Examination of these results shows that the rotor sees the flux due to the 5th harmonic current as a backwards-rotating flux wave at the 6th harmonic frequency, and the 7th harmonic flux as a forwards-rotating flux wave also at the 6th harmonic frequency. Since the rotor core losses are eddy current dominated at the frequencies of interest, linearity implies that the losses for each harmonic component can be analyzed individually. The losses can then be estimated by analyzing the case of a traveling wave of the appropriate amplitude impinging on a solid steel sheet.

An analytical expression for the losses has been derived in [13] based on transfer function relations found in [14]. The result is:

$$P_{loss} = S\frac{|K|^2}{\delta_h\sigma(b\cosh bg)^2}, \quad b = \frac{m}{r} \quad (16)$$

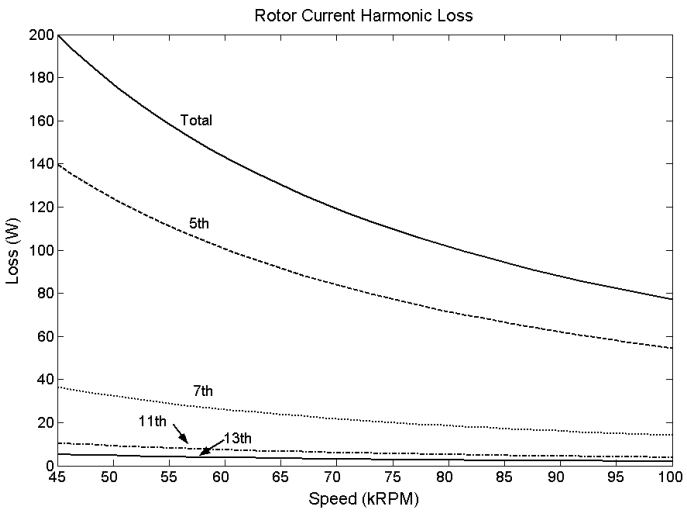

Fig. 15. Rotor current harmonics losses.

where S is the surface area, K is the linear current density in *A/m* along the inner bore of the stator, δ_h is the skin depth for the material at ω_e, r is the rotor radius, g, is the gap, and m is the spatial harmonic. Since the skin depth $\delta_h << g$, the problem can be transformed into rectilinear coordinates. The constant b is a result of the coordinate transformation, and m=(# of poles)/2. The results from this expression agree with 2D FEM simulations of the rotor profile conducted at lower frequencies (1 kHz). Accurate FEM simulations at the frequencies of interest in our design ($\omega_e > 2\pi\cdot 18$kHz) are difficult because the skin depths (26μm at 18kHz) are very small compared to the air gap (2.16 mm) and other rotor geometry.

Fig. 15 plots the losses calculated for the 5th, 7th, 11th, and 13th harmonics along with the total loss for all harmonics for the target operating speed range with $V=285V$ and $L_A = 78\ \mu H$. Note that the harmonic losses decrease with increasing speed, and the worst case is 175 W which occurs at 50,000 RPM. The average losses under normal operating cycles would be smaller. A calculation of the rotor's thermal radiation indicates that 175 W of rotor loss with a stator temperature of 50°C would imply a rotor operating temperature of approximately 200°C, which is reasonable for a solid steel rotor.

A-III Sizing of Armature Inductance L_A

As noted in the previous two sections, increasing armature inductance L_A decreases losses due to the harmonics generated from a six-step drive; however, this comes at the expense of decreasing the machine power factor and the overall efficiency of the machine. One approach to constraining L_A is to choose a maximum acceptable amplitude for one of the harmonic currents and a minimum machine power factor.

Define I_5 to be the amplitude of the fifth harmonic current (the primary source of harmonic losses), and θ_{pf} to be the angle to achieve the machine power factor $\cos\theta_{pf}$. Then choose β such that satisfying the inequality:

$$I_5 < \beta\cdot I_{A1} \quad (17)$$

leads to small enough harmonic currents such that the harmonic conduction and rotor losses are acceptable. Then

substituting in the expression for the amplitude of the fifth harmonic component of the current from (15) for I_5 leads to the expression:

$$\frac{1}{\beta \cdot 5^2} < \frac{\omega_e L_A I_{A1}}{V} \tag{18}$$

Now a constraint for the minimum machine power factor will be developed. From the phasor diagram in Fig. 4, where the inverter is running at unity power factor and the machine power factor angle is θ, the machine power factor will be greater than $\cos\theta_{pf}$ if:

$$\frac{\left| j\omega_e L_A I_{A1} \right|}{V} < \tan\theta_{pf} \tag{19}$$

Combining (18), (19), and $P=3/2 \cdot I_{A1} V$ results in:

$$\frac{1}{\beta \cdot 5^2} < \frac{2\omega_e L_A P}{3V^2} < \tan\theta_{pf} \tag{20}$$

This expression helps to guide the choice of L_A so that the harmonic losses can be limited to some maximum value while a minimum machine power factor at peak power is also maintained. Note that in a six-step drive where V is fixed, the ratio of the maximum speed over minimum speed is constrained by:

$$\frac{\omega_{e,\max}}{\omega_{e,\min}} < \beta \cdot 5^2 \cdot \tan\theta_{pf} \tag{21}$$

Given the desired 2:1 speed range, and using $\beta=0.10$ (the value used for the example plotted in Fig. 14 which corresponds to V=285V, P=30kW, L_A=78μH), then (21) implies a minimum power factor of 0.78. This minimum power factor occurs at full power at $\omega_{e,max}$, while at full power at $\omega_{e,min}$ the power factor would be 0.93.

A-IV Winding Harmonic Loss Analysis

Calculations for the losses associated with spatial winding harmonics ('belt harmonics') can be calculated in a similar fashion to the current harmonic losses. The prototype motor has a trapezoidal winding MMF, and the surface current K_A of phase A with current I_A flowing can also be expressed in terms of its Fourier components as:

$$K_A = \frac{I_A}{W}\cos(\omega_e t) \sum_{m=1,3,5\ldots} K_m \cos(\theta) \tag{22}$$

where θ is the spatial angle along the bore of the motor, W the width of one turn, and K_m the amplitude of the m^{th} harmonic. The sum of the surface currents for the three phases is the resultant MMF:

$$K_{tot} = K_A + K_B + K_C \tag{23}$$

It can be shown that when balanced three phase sinusoidal currents I_a, I_b, and I_c, of equal amplitude $|I|$ are applied and K_{tot} is expressed in the rotor frame, K_{tot} can be expressed as a sum of $6i$ time harmonics [13]:

$$\begin{aligned} K_{tot} = \frac{3}{2}\frac{|I|}{W}\Big[& K_1 \cos\theta \\ & + \sum_{i=1,2,3\ldots} K_{6i-1}\cos((6i-1)\theta + 6i\omega_e t)) \\ & + \sum_{i=1,2,3\ldots} K_{6i+1}\cos((6i+1)\theta + 6i\omega_e t))\Big] \end{aligned} \tag{24}$$

Since these losses also appear as traveling waves at the 6th harmonic frequency, the losses can be analyzed using (16), with the modification of b such that:

$$b = \frac{m \cdot l}{r},\ l = 5,7,11,13\ldots \tag{25}$$

to reflect the change in the spatial wavelength of the harmonic. The rotor losses from the winding harmonics are much smaller than the losses from the current harmonics. There are two reasons for this. First, the spatial MMF patterns are trapezoidal for each phase, significantly reducing the 5th and 7th harmonic amplitudes relative to a square-wave MMF pattern. Second, the spatial wavelength for the winding harmonic induced MMF impinging on the rotor is one-sixth that which corresponds to the fundamental wavelength, resulting in reduced flux penetration into the rotor volume. In the worst case, these losses are estimated at less than 1W. The above spatial harmonic analysis only considers the losses from spatial harmonics driven by the fundamental current. The losses from spatial harmonics due to harmonic currents (e.g. 5th spatial harmonic with 7th current harmonic) will have a negligibly small contribution to the total loss.